Inversion-Asymmetry Splitting of the Conduction Band in GaSb from Shubnikov–de Haas Measurements*

D. G. Seiler† AND W. M. Becker

Department of Physics, Purdue University, Lafayette, Indiana 47907

AND

Laura M. Roth

General Electric Research and Development Center, Schenectady, New York 12301

(Received 15 September 1969)

A detailed experimental investigation has been carried out on the beating patterns seen in the Shubnikov–de Haas (SdH) oscillations in Te-doped n-GaSb. Samples with Hall coefficients $R_{4.2^\circ K} = -5.5$ cm³/C to $R_{4.2^\circ K} = -3.2$ cm³/C were studied. Typical behavior is seen in a sample with $R_{4.2^\circ K} = -3.2$ cm³/C, where nodes or minima in the oscillatory amplitude occur at ~ 11 kG and ~ 4.8 kG for $\mathbf{B} \| \langle 111 \rangle$, and at ~ 6.5 kG for $\mathbf{B} \| \langle 001 \rangle$; no minima are observed for $\mathbf{B} \| \langle 110 \rangle$. The low-field results are in contrast to high-field behavior in which only approximately exponential field dependence of the oscillatory amplitude is obtained. These patterns are similar to those observed by Whitsett in the SdH effect in n-HgSe. We analyze the results in GaSb initially in terms of a classical model of two Fermi surfaces split by inversion asymmetry. This model qualitatively predicts some features of the data, including the concentration dependence of the highest-field nodal point seen with $\mathbf{B} \| \langle 111 \rangle$. Finally, we compare the data with predictions of a nonclassical model involving interaction between electron spin and external magnetic fields. The nonclassical model correctly predicts the nodal positions in GaSb, using a value of the splitting parameter $C_2 = 0.05$, where $C_2 E_F$ is the maximum energy splitting at the Fermi surface. For a sample $R_{4.2^\circ K} = -3.2$ cm³/C ($E_F \simeq 0.096$ eV), the maximum splitting is 0.005 eV. The analysis further yields a value for the higher-band matrix element sum B' (Kane's B) $\approx 9.6 \hbar^2/2m_0$.

I. INTRODUCTION

UNTIL recently, studies of the Shubnikov–de Haas (SdH) effect in n-type Te-doped GaSb were confined to using magnetic fields above 18 kG.[1-5] Seiler and Becker (SB)[6] used ac magnetic field modulation and phase-sensitive detection techniques to study SdH oscillations down to about 4 kG in the highest-concentration samples of GaSb available. These techniques made possible the first observation of beating effects in the SdH oscillations in this material. It was suggested in SB that these beating effects might be ascribed to inversion-asymmetry splitting of the $k = 0$ conduction band. This suggestion was based on the remarkable similarity of the results to the observed beating effects in HgSe,[7] and on the theoretical arguments of Roth, Groves, and Wyatt (RGW)[8] in explaining the HgSe data.

The theory of the inversion-asymmetry terms in energy-band theory in zinc-blende crystals has been known for some time.[9,10] These terms result from the antisymmetric potential or inversion asymmetry of the zinc-blende lattice. Combined with the spin-orbit interaction, these terms split the twofold energy degeneracy at a general value of k. Because the splittings are so small, they have been difficult to observe experimentally.

Robinson[11] reported results of cyclotron resonance measurements on p-type InSb; he invoked inversion-asymmetry splitting to explain the data. Recently, RGW proposed that the SdH measurements of Whitsett on n-type HgSe demonstrate these zinc-blende splittings. Whitsett found that when $\mathbf{B}$ is rotated in a $\{110\}$ plane, beating occurs for directions of $\mathbf{B}$ away from the $\langle 110 \rangle$ directions in samples of sufficiently high electron concentration. When $\mathbf{B}$ is along a $\langle 100 \rangle$ direction, a single node is observed in the range of field strength studied; for $\mathbf{B}$ along a $\langle 111 \rangle$ direction, one or two nodes are observed. Beating does not occur for $\mathbf{B}$ along a $\langle 110 \rangle$ direction. The anisotropy of the period was found to be quite small. Groves and Wyatt[12] used this result to rule out another possible explanation of the beating, namely a severe warping of the Fermi surface. More recently, Roth (R)[13] has calculated the magnetic energy levels in an energy band with inversion-asymmetry splitting. This calculation provided further evidence in support of the initial proposal of RGW that the beating effects in HgSe are due to inversion-asymmetry splitting.

In this paper, we shall present the results obtained from a comprehensive experimental study of the beating effects in n-GaSb(Te). These include a systematic study of the concentration dependence of the nodal positions, the variation of the nodal positions with magnetic field direction, and the amplitude dependence of the oscillations at high fields. It will be shown that certain features

[1] W. M. Becker and H. Y. Fan, in *Proceedings of the International Conference on the Physics of Semiconductors* (Dunod Cie., Paris, 1964), p. 663.

[2] T. O. Yep and W. M. Becker, Phys. Rev. **144**, 741 (1966).

[3] T. O. Yep and W. M. Becker, Phys. Rev. **156**, 939 (1967).

[4] A. I. Ponomarev and I. M. Tsidil'kovskii, Soviet Phys.—Semicond. **1**, 1375 (1968).

[5] D. V. Mashovets, R. V. Parfen'ev, and V. S. Vekshina, Fiz. Tverd. Tela **10**, 3417 (1968) [English transl.: Soviet Phys.—Solid State **10**, 2700 (1969)].

[6] D. G. Seiler and W. M. Becker, Phys. Letters **26A**, 96 (1967).

[7] C. R. Whitsett, Phys. Rev. **138**, A829 (1965).

[8] L. M. Roth, S. H. Groves, and P. W. Wyatt, Phys. Rev. Letters **19**, 576 (1967).

[9] R. H. Parmenter, Phys. Rev. **100**, 573 (1955).

[10] G. Dresselhaus, Phys. Rev. **100**, 580 (1955).

[11] M. L. Robinson, Phys. Rev. Letters **17**, 963 (1966).

[12] S. H. Groves and P. W. Wyatt, calculation discussed in Refs. 8 and 13 (unpublished).

[13] L. M. Roth, Phys. Rev. **173**, 755 (1968).

of the beating behavior cannot be explained in terms of a classical model of two Fermi surfaces produced by inversion-asymmetry splitting of the $k=0$ conduction band. The experimental results can be explained by the theory given in R, which predicts nonclassical behavior of the two electron orbits on the two Fermi surfaces.

II. THEORY

A. Classical Areas and SdH Frequencies

The consequence of inversion-asymmetry splitting in the conduction band of GaSb or HgSe is the prediction that there are two different energy surfaces corresponding to the same Fermi energy. The constant-energy contours of the split bands in the $\mathbf{k}_H = 0$ plane for $\mathbf{k}_H$ or $\mathbf{B}$ parallel to $\langle 100 \rangle$, $\langle 110 \rangle$, and $\langle 111 \rangle$ directions have been calculated in RGW by computer techniques for the case of HgSe. It is easier to use the techniques of Seiler and Becker (SB)[14] to calculate the area difference between these two classical orbits. In SB, Kane's[15] "three-band approximation," which included the higher-band $\mathbf{k} \cdot \mathbf{p}$ interactions, was used to derive an analytic expression for the SdH frequencies for GaSb in terms of the Fermi energy, band parameters, and magnetic field direction. Their results showed that only the warping term need be considered in analyzing the observed SdH frequency anisotropy. The contribution of the inversion-asymmetry term was, thus, not considered. We now include this inversion-asymmetry splitting term in the energy and proceed to derive the classical SdH frequencies using the same techniques presented in SB.

In SB, it was shown that the Γ_6 conduction-band energy of GaSb relative to the conduction-band minimum could be written in the form

$$E_4{}^{\pm} = -\tfrac{1}{2}E_g + \tfrac{1}{2}E_g\left(1 + \frac{4k^2P^2(E_g + 2\Delta/3)}{E_g{}^2(E_g + \Delta)}\right)^{1/2}$$
$$+ \frac{uh^2k^2}{2m_0} + \frac{vf_1(\mathbf{k})h^2}{2m_0} \pm \frac{wf_2(\mathbf{k})h^2}{2m_0}. \quad (1)$$

In Eq. (1), P is the momentum matrix element, E_g is the direct energy gap at $k=0$, Δ is the energy splitting of the valence band due to the spin-orbit interaction, and

$$f_1(\mathbf{k}) = (k_x{}^2k_y{}^2 + k_x{}^2k_z{}^2 + k_y{}^2k_z{}^2)/k^2, \quad (2)$$

$$f_2(\mathbf{k}) = [k^2(k_x{}^2k_y{}^2 + k_x{}^2k_z{}^2 + k_y{}^2k_z{}^2) - 9k_x{}^2k_y{}^2k_z{}^2]^{1/2}/k. \quad (3)$$

The coefficients u, v, and w are defined by

$$u = 1 + a_4{}^2A' + b_4{}^2M + c_4{}^2L', \quad (4)$$

$$v = (b_4{}^2 - 2c_4{}^2)(L - M - N), \quad (5)$$

and

$$w = \sqrt{2}a_4b_4B'. \quad (6)$$

[14] D. G. Seiler and W. M. Becker, Phys. Rev. **183**, 784 (1969).
[15] E. O. Kane, in *Semiconductors and Semimetals*, edited by R. K. Willardson and A. C. Beer (Academic Press Inc., New York, 1966), Vol. 1, p. 75.
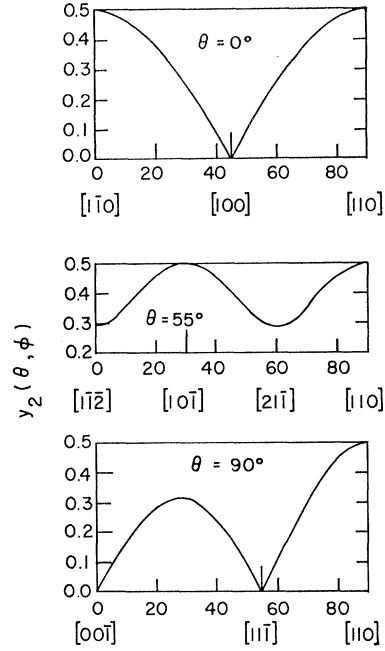

FIG. 1. Plots of $y_2(\theta, \varphi)$ versus φ, for $\theta = 0°$, $\theta = 55°$, and $\theta = 90°$ for $\mathbf{B}$ lying in the (110) plane.

The normalized coefficient a_4 gives the amount of s-like basis function in the conduction-band eigenvector, and the normalized coefficients b_4 and c_4 give the amounts of different component p-like basis functions in the conduction-band eigenvector. The parameters A', L, M, N, L', and B' (Kane's B), written in units of $h^2/2m_0$, represent the interaction between far-removed conduction and valence-band edges and the s- and p-like bands. The term $f_1(\mathbf{k})$ produces a warping of the Fermi surface and the term $f_2(\mathbf{k})$ is the inversion-asymmetry splitting term with which we are concerned here. For very small k, the energy goes as k^2, as is well known. The inversion-asymmetry term is of order k^3 for small k, and the warping term comes in with terms of order k^4.

The possibility that warping in diamond and in zinc-blende semiconductors is sufficiently large to result in extremal cross-section areas away from $\mathbf{k}_H = 0$ (where $\mathbf{k}_H$ is parallel to the magnetic field direction) has been discussed in RGW. From their discussion, and the result that the warping found in SB is very small, it can be concluded that the maximum cross-section area perpendicular to the magnetic field occurs at $\mathbf{k}_H = 0$.

If the coordinate system is rotated to put the magnetic field along the z direction, and the transformed k_z set equal to zero as described in SB, we get the following expression for the conduction-band energy:

$$E_4{}^{\pm} = -\tfrac{1}{2}E_g + \tfrac{1}{2}E_g\left(1 + \frac{4k_{\rho\pm}{}^2P^2(E_g + 2\Delta/3)}{E_g{}^2(E_g + \Delta)}\right)^{1/2}$$
$$+ \frac{uh^2k_{\rho\pm}{}^2}{2m_0} + \frac{vy_1(\theta, \varphi)h^2k_{\rho\pm}{}^2}{2m_0} \pm \frac{wy_2(\theta, \varphi)h^2k_{\rho\pm}{}^2}{2m_0}. \quad (7)$$
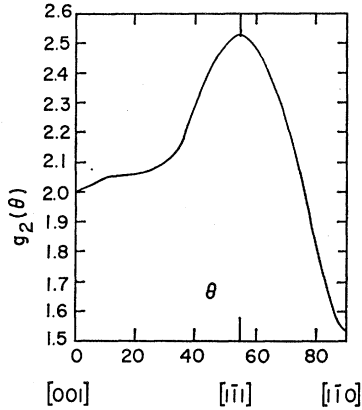
FIG. 2. Plot of $g_2(\theta)$ versus θ for $\mathbf{B}$ lying in the (110) plane.

The quantities $k_{\rho\pm}$ and φ are a set of polar coordinates lying in the plane perpendicular to the magnetic field $\mathbf{B}$, and θ is the angle between the field direction and a crystallographic direction lying in the plane of rotation of the magnetic field. The form of the functions $y_1(\theta,\varphi)$ and $y_2(\theta,\varphi)$ depends on the plane of rotation of the magnetic field. The form of $y_1(\theta,\varphi)$ for the magnetic field lying in a $\{110\}$ plane is given in Appendix A of SB. The form of $y_2(\theta,\varphi)$ is obtained in a similar way by the use of the transformation equations given in Eq. (A2) in SB:

$$y_2(\theta,\varphi) = \{(9/4)\cos^6\varphi[-1-\cos^2\theta+\cos^4\theta+\cos^6\theta]$$
$$+\tfrac{1}{4}\cos^4\varphi[+15+10\cos^2\theta-21\cos^4\theta]$$
$$+\tfrac{1}{4}\cos^2\varphi[-7+3\cos^2\theta]+\tfrac{1}{4}\}^{1/2}. \quad (8)$$

Plots of $y_2(\theta,\varphi)$ versus φ for $\theta=0°$, $55°$, and $90°$ (i.e., the magnetic field parallel to the [001], [1$\bar{1}$1], and [1$\bar{1}$0] directions, respectively) are given in Fig. 1.

Using the method presented in SB, one can then show that the two k vectors are given by

$$k_{\rho\pm}^2 \approx C_0[1-C_1 y_1(\theta,\varphi)\mp C_2 y_2(\theta,\varphi)], \quad (9)$$
where
$$C_0 = \frac{2m_0}{\hbar^2}(E_4^{\pm 2}+E_4^{\pm}E_g)/D, \quad (10)$$

$$C_1 = (2E_4^{\pm}+E_g)v/D, \quad (11)$$
and
$$C_2 = (2E_4^{\pm}+E_g)w/D, \quad (12)$$
where
$$D = \frac{P^2(E_g+2\Delta/3)}{(E_g+\Delta)(\hbar^2/2m_0)}+(2E_4^{\pm}+E_g)u. \quad (13)$$

The coefficients C_0, C_1, and C_2 are only dependent on the Fermi energy and the band parameters. Thus, the extremal cross-section areas, $\mathcal{Q}_\pm$, perpendicular to the magnetic field are given by

$$\mathcal{Q}_\pm = \pi C_0[1-(C_1/2\pi)g_1(\theta)\mp(C_2/2\pi)g_2(\theta)], \quad (14)$$

where $g_1(\theta)=\int_0^{2\pi} y_1(\theta,\varphi)d\varphi$ and is shown in Appendix A in SB. The integral $g_2(\theta)=\int_0^{2\pi} y_2(\theta,\varphi)d\varphi$ has been

calculated by numerical integration with the aid of a computer, and is shown in Fig. 2. The SdH frequencies contributed by the two areas are

$$F_\pm(\theta) = \frac{\hbar c C_0}{2e}[1-(C_1/2\pi)g_1(\theta)\mp(C_2/2\pi)g_2(\theta)]. \quad (15)$$

The classical result for the beat frequency is the difference between the two frequencies of Eq. (15),

$$F_B = F_0(C_2/\pi)g_2(\theta), \quad (16)$$

where $F_0=\hbar c C_0/2e$ is the SdH frequency obtained by ignoring inversion asymmetry (and anisotropy also). The number of oscillations between nodes is F_0/F_B.

The cyclotron resonance effective masses $m_\pm^*$ can be calculated using the same techniques presented in SB. The resulting equation for $m_\pm^*$ is

$$m_\pm^* \cong \tfrac{1}{2}\hbar^2 K_0[1-(K_1/2\pi)g_1(\theta)\mp(K_2/2\pi)g_2(\theta)], \quad (17)$$

where

$$K_0 = (rE_gP^2-2r^2E_gP^4C_0+6r^3E_gP^6C_0^2+u\hbar^2/2m_0), \quad (18)$$

$$K_1 = (2r^2E_gP^4C_0C_1-12r^3E_gP^6C_0^2C_1+v\hbar^2/2m_0)K_0, \quad (19)$$

$$K_2 = (2r^2E_gP^4C_0C_2-12r^3E_gP^6C_0^2C_2+w\hbar^2/2m_0)K_0, \quad (20)$$

and

$$r = (E_g+2\Delta/3)/E_g^2(E_g+\Delta). \quad (21)$$

The constant energy contours of the split bands are easily calculated. Since the warping and inversion-asymmetry terms are small, the constant-energy contours are almost circular. It is desirable to plot a quantity which shows departures from a spherical Fermi surface due to both warping and inversion-asymmetry splitting. This is conveniently done by defining as an index of deviation from sphericity the quantity

$$\chi_\pm = \frac{k_{\rho\pm}(\varphi)-k_{\rho\pm}(001)}{k_{\rho\pm}(001)}+0.01. \quad (22)$$

From Eq. (9),

$$k_{\rho\pm} \approx C_0^{1/2}[1-(C_1/2)y_1(\theta,\varphi)\mp(C_2/2)y_2(\theta,\varphi)], \quad (23)$$

for a given θ. Thus,

$$\chi_\pm \approx \tfrac{1}{2}[-C_1 y_1(\theta,\varphi)\mp C_2 y_2(\theta,\varphi)]+0.01. \quad (24)$$

[The factor of 0.01 has been added to ensure that $\chi_\pm>0$, which is convenient in making polar plots of $\chi_\pm$]. Plots of $\chi_\pm$ for the $k=0$ conduction band of GaSb are shown in Fig. 3 for $\mathbf{B}\|[1\bar{1}0]$, [1$\bar{1}$1], and [001]. A value of $C_1(-0.086)$ obtained from the warping analysis given in SB was used in Eq. (24). A value of $C_2(0.05)$ obtained from fitting the quantum-mechanical theory to the experimental data (below) was also used. It can be seen from Fig. 3 that the splitting of the two surfaces vanishes for $\mathbf{k}$ along the $\langle 111\rangle$ and $\langle 110\rangle$ directions, as expected. The size of the splittings in a particular $\mathbf{k}$ direction can be estimated from the figures; this gives the fractional
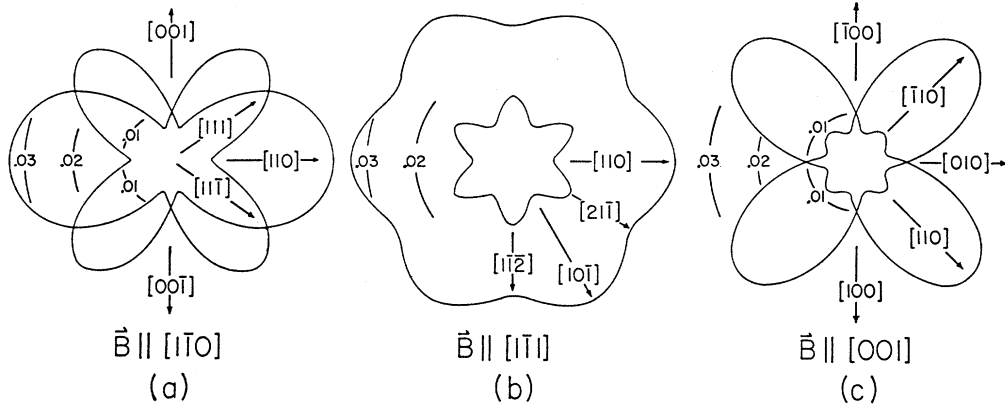
FIG. 3. Polar plots of $\chi_{\pm}=[k_{\rho\pm}(\varphi)-k_{\rho\pm}(001)]/k_{\rho\pm}(001)+0.01$. Three cases are shown: (a) $\theta=90°$; (b) $\theta=55°$; (c) $\theta=0°$. The data are plotted using $C_1=-0.086$ and $C_2=0.05$. The scale markings indicate the magnitude of $\chi_{\pm}$.

difference in **k**-vectors between the two surfaces. Alternatively, use of Eqs. (22) and (23) gives

$$\chi_- - \chi_+ = k_{\rho-}(\varphi) - k_{\rho+}(\varphi)/k_{\rho\pm}(001) = C_2 y_2(\theta,\varphi). \quad (25)$$

When the **k** vector is parallel to a $\langle 110 \rangle$ direction, $y_2(\theta,\varphi)$ has its maximum value of 0.5, and the splitting of the two Fermi surfaces is a maximum, as seen in Fig. 3. The splitting $\Delta\chi$ is $\frac{1}{2}C_2$ for this direction.

For a constant **k** value the energy splitting near the Fermi level E_F can be estimated using Eq. (7), which gives

$$E_4^+ - E_4^- = 2wy_2(\theta,\varphi)(\hbar^2 k_\rho{}^2/2m_0)$$
$$= 2wy_2(\theta,\varphi)(\hbar^2 k_\rho{}^2/2m^*)(m^*/m_0). \quad (26)$$

Since

$$E_F \approx \frac{\hbar^2 k^2}{2m^*},$$

and

$$C_2 \approx \left(\frac{m^*}{m_0}\right)w, \quad (27)$$

$$E_4^+ - E_4^- \approx 2C_2 y_2(\theta,\varphi)E_F.$$

The maximum $(\mathbf{k}\|\langle 110\rangle)$ energy splitting near the Fermi level E_F is then approximately $C_2 E_F$.

B. Quantum-Mechanical Theory

In this section, an extensive review of the quantum mechanical theory explaining the beating effects in HgSe is presented. This theory is directly applicable to the case of GaSb.

Even though beating effects are predicted by the classical theory, it was shown in R that quantum effects must be included to obtain quantitative agreement with the experimental results. There are two principal reasons for considering quantum effects. First, in symmetry directions, extremal orbits go through conical points where the two Fermi surfaces touch, and classical considerations do not predict whether the electron goes through to the other surface or makes an abrupt turn

and stays on the same Fermi surface. By considering quantum effects, it is found that an electron goes through the conical point in the classical region of small magnetic fields. However, within the range of experimental magnetic fields, serious departures from the classical results are found. In the vicinity of the conical points, magnetic-breakdown effects occur. Secondly, even away from these conical points, the electron orbits for the two Fermi surfaces are very close together and there is always an interaction between them.

In order to treat the problem quantum mechanically, we use Luttinger's[16] manner of constructing an effective one-band Hamiltonian. This Hamiltonian depends upon spin and wave vector and can be written as

$$H(\boldsymbol{\sigma},\mathbf{k}) = \epsilon_0(k^2) + [\hbar\omega_s(\boldsymbol{\sigma}\cdot\mathbf{B})/2B]$$
$$+ (w\hbar^2/2m_0)[g(\boldsymbol{\sigma},\mathbf{k})/k]. \quad (28)$$

Here, ϵ_0 contains the first two terms of Eq. (1). The second term in Eq. (28) is the Zeeman interaction, where $\hbar\omega_s$ is the spin splitting and $\boldsymbol{\sigma}$ is a Pauli spin vector. The warping term [the $f_1(\mathbf{k})$ term in Eq. (1)], which was considered in detail in SB will be neglected in this analysis. The last term in Eq. (28) is the inversion-asymmetry term and replaces the last term of Eq. (1). The definition of w is the same as given in Eq. (6), and

$$g(\boldsymbol{\sigma},\mathbf{k}) = (\sigma_x k_y - \sigma_y k_x)k_x k_y + (\sigma_y k_z - \sigma_z k_y)k_y k_z$$
$$+ (\sigma_z k_x - \sigma_x k_z)k_z k_x. \quad (29)$$

The form of Eq. (29) is deduced from the fact that it must be invariant under the tetrahedral group and under time-inversion invariance. Its appearance depends, of course, upon the lack of inversion symmetry. For small k, w/k approaches a finite value and the k^3 dependence of Eq. (29) is carried over to the inversion-asymmetry term of Eq. (28).

The eigenvalues of $g(\boldsymbol{\sigma},\mathbf{k})$ in zero magnetic field are $\pm k f_2(\mathbf{k})$, where $f_2(\mathbf{k})$ was defined in Eq. (3). For a finite

[16] J. M. Luttinger, Phys. Rev. **102**, 1030 (1956).

magnetic field, $\mathbf{k}$ must be interpreted as the operator

$$\hbar\mathbf{k} = (\hbar/i)\nabla + [e\mathbf{A}(\mathbf{r})/c], \qquad (30)$$

where $\mathbf{A}(\mathbf{r})$ is the vector potential of the magnetic field. The commutation relations between the components are

$$[k_x,k_y] = -ieB_z/\hbar c. \qquad (31)$$

In general, the ordering of the factors of the $\mathbf{k}$ components is important. However, the inversion-asymmetry term is small and, hence, the order of the factors of k in the inversion-asymmetry term can be neglected.

In R, it was shown that Eq. (28) is equivalent, in the vicinity of the Fermi level, to the parabolic band Hamiltonian

$$H_{\text{par}} = (\hbar^2 k^2/2m^*) + (\hbar\omega_s \boldsymbol{\sigma}\cdot\mathbf{B}/2B)$$
$$+ (C_2\hbar^2/2m^*k_F)g(\boldsymbol{\sigma},\mathbf{k}), \qquad (32)$$

where C_2 is given by Eq. (12) and is the same as the γ of R and RGW used earlier. Here, m^* is the effective mass at the Fermi level. Equation (32) can now be transformed to a coordinate system in which the magnetic field is in the z direction, as discussed in the classical theory. However, here $\boldsymbol{\sigma}$ as well as $\mathbf{k}$ must be transformed using the transformation techniques presented in Appendix A of SB. After setting $k_z''=0$ and dropping the primes, the transformed form of Eq. (29) yields

$$g(\boldsymbol{\sigma},\mathbf{k}) = \sigma_z \sin\theta k_y[(2+3\cos^2\theta)k_x^2 - k_y^2]$$
$$+ (\sigma_x k_y - \sigma_y k_x)\cos\theta[(-2+3\cos^2\theta)k_x^2 - k_y^2], \qquad (33)$$

where θ is the angle between the magnetic field and a cube axis.

The problem reduces to a set of coupled differential equations for the effective-mass wave functions ψ_1 and ψ_2. To be explicit we write them out:

$$\left\{\frac{\hbar^2}{2m^*}(k_x^2+k_y^2)+\tfrac{1}{2}\hbar\omega_s\right.$$

$$\left.+\frac{\hbar^2 C_2}{2m^*k_F}sk_y[(3c^2+2)k_x^2-k_y^2]\right\}\psi_1(x,y)$$

$$+\left\{\frac{\hbar^2}{2m^*k_F}i(k_x-ik_y)c[(3c^2-2)k_x^2-k_y^2]\right\}\psi_2(x,y)$$

$$= E_{\text{par}}\psi_1(x,y), \qquad (34)$$

$$\left\{\frac{\hbar^2}{2m^*k_F}i(k_x+ik_y)c[(3c^2-2)k_x^2-k_y^2]\right\}\psi_1(x,y)$$

$$+\left\{\frac{\hbar^2}{2m^*}(k_x^2+k_y^2)-\tfrac{1}{2}\hbar\omega_s\right.$$

$$\left.-\frac{\hbar^2}{2m^*k_F}C_2sk_y[(3c^2+2)k_x^2-k_y^2]\right\}\psi_2(x,y)$$

$$= E_{\text{par}}\psi_2(x,y). \qquad (35)$$

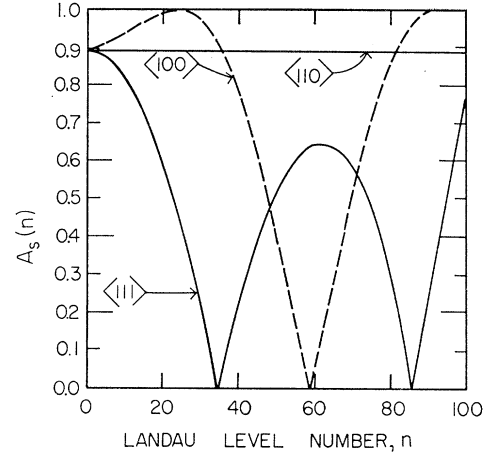

FIG. 4. Plot of $A_s(n)$ versus n.

Here, $s=\sin\theta$ and $c=\cos\theta$. The form of the differential operators depends on the gauge. For example, if $A=(0,Bx,0)$ and $\psi=e^{ik_y}\varphi(x)$, we have $k_x=(1/i)(\partial/\partial x)$, and $k_y=k_y-(eBx/c)$. The unperturbed problem ($C_2=0$) has eigenvalues $\hbar\omega_c(n+\tfrac{1}{2})\pm\tfrac{1}{2}\hbar\omega_s$.

In R we succeeded in solving these equations only for $\mathbf{B}$ along the three principal crystallographic directions. The simplest case was for $\mathbf{B}\|\langle110\rangle$, where $s=1$ and $c=0$. In this case, the coupling term between the two ψ's vanishes, so that the equations are independent and can be solved classically. As the classical orbits are of equal areas, there is no beating, and the electrons take paths through the conical points on the Fermi surface.

For $\mathbf{B}$ along the $\langle100\rangle$ and $\langle111\rangle$ directions, several transformations were made and ψ_1 and ψ_2 were expanded in terms of a finite but large set of harmonic-oscillator functions. The resulting matrix simplified in such a way that the secular determinant could be readily evaluated and the eigenvalues obtained. We shall not go into details but refer the reader to the article. The two parameters of importance are C_2 and $\mu=\tfrac{1}{2}(1-\omega_s/\omega_c)$ $=\tfrac{1}{2}(1-gm^*/2m_0)$. (Please note the misprint in R, p. 761.) The numerous eigenvalues can be grouped into two sets which are very close to the unperturbed harmonic-oscillator levels. We can, therefore, label them by the unperturbed quantum number n, and we write for the two sets

$$\epsilon_1(n) = [n+\tfrac{1}{2}+\delta_1(n)]\hbar\omega_c,$$
$$\epsilon_2(n) = [n+\tfrac{1}{2}+\delta_2(n)]\hbar\omega_c. \qquad (36)$$

Here, $\delta_1(n)$ and $\delta_2(n)$ are relatively slowly varying functions of n which contain the effects of spin splitting as well as inversion asymmetry. The variation of δ_1 and δ_2 with n produces beating in the SdH effect; the nodes occur for $\delta_1-\delta_2=\tfrac{1}{2}$ modulo 1, in which case the levels are interleaved.

The function modulating the SdH amplitude of the fundamental frequency due to inversion-asymmetry

splitting is given by

$$A_s(n) = \cos\pi[\delta_1(n) - \delta_2(n)]. \qquad (37)$$

This multiplies the quantity $A_T(B)$ in Eq. (7) in SB and produces the beat pattern. Since Eq. (37) already contains the spin splitting, the spin splitting included in $A_T(B)$ must be deleted for a correct calculation of the amplitude. The B dependence of $A_s(n)$ can be found with the help of Eq. (36). Thus, if the ϵ's are constant then the levels come at equal intervals (except for δ) of $\epsilon/\hbar\omega_c$. These levels correspond to the oscillations in the magnetoresistance, so that the variable n (or oscillation number) corresponds to the variable $1/B$ measured in units of the SdH period.

A plot of $A_s(n)$ versus n for $\mathbf{B}$ along the $\langle 111 \rangle$ and $\langle 100 \rangle$ directions is shown in Fig. 4 for parameters fitting the experimental nodes. There is one node in the $\langle 100 \rangle$ case, straddled by two nodes, in the range of interest, in the $\langle 111 \rangle$ case. This reproduces the experimental pattern for GaSb and HgSe. We shall go further into the details of the fit in Sec. V and only remark here that for small n, or large B, A_s approaches the value $\cos(\pi g m^*/2m_0)$.

III. EXPERIMENTAL WORK

The single-crystal ingots of GaSb were grown by the Czochralski method, with sufficient Te being added to the stoichiometric melt to produce n-type material with electron concentrations of about 10^{18} cm^{-3}. The ingots were then oriented using x-ray diffraction techniques. To reduce the effects of inhomogeneities, rectangular shaped samples were taken from slices cut perpendicular to the crystal growth direction.

Magnetic field modulation and phase-sensitive detection techniques were employed in the SdH measurements at low magnetic fields. This low-frequency field modulation modifies the usual amplitude of the SdH oscillations by introducing a series of terms involving Bessel functions.[17,18] This series is reduced to a single term by using a lock-in amplifier detecting at a harmonic of the modulation frequency. A 4-in. Pacific Electric Motor electromagnet provided fields up to 22 kG. A Rawson rotating coil fluxmeter, which had been previously calibrated using an NMR probe, was used to measure the magnetic field strength. Higher fields up to 80 kG were made available by using a Westinghouse superconducting magnet, and a high-field pulse solenoid provided fields up to approximately 190 kG.

IV. EXPERIMENTAL RESULTS

Figure 5 (taken from Ref. 6) shows low-field oscillatory data taken at 1.4°K on sample 24B for several field directions transverse to the current direction. The

[17] A. Goldstein, S. J. Williamson, and S. Foner, Rev. Sci. Instr. 36, 1356 (1965).
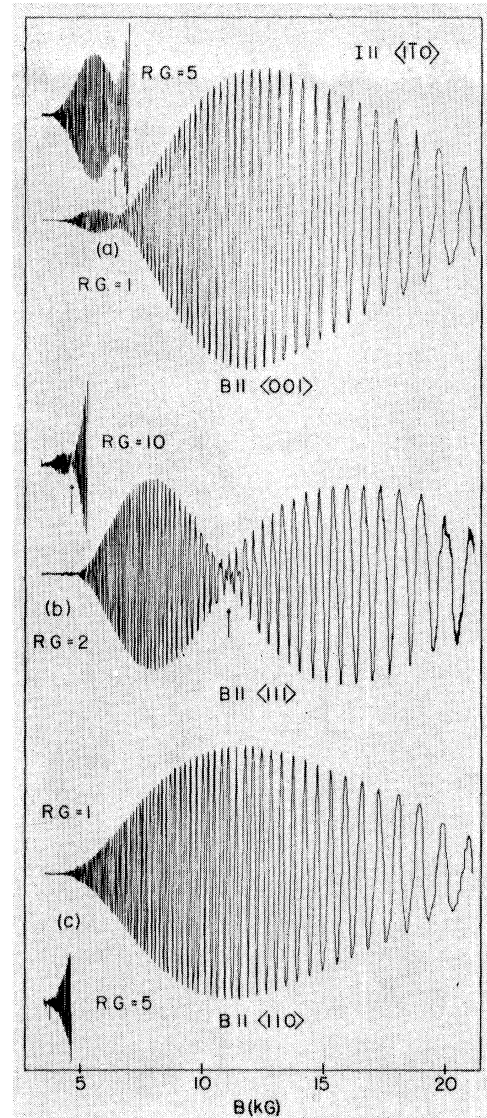[18] B. L. Booth, Ph.D. thesis, Northwestern University, 1967 (unpublished).

Fig. 5. Reproduction of x-y recorder traces of oscillatory magnetoresistance data taken on sample 24B while detecting at the second harmonic of the modulation frequency. The RG of each trace is indicated. This figure is taken from Ref. 6, Fig. 1.

relative gain (RG) of each trace is indicated. The traces taken at higher gain have been slightly displaced for clarity. The arrows show the approximate field positions of the observed minima. Detection at the second harmonic of the frequency of the modulation field B_M multiplies the usual oscillatory amplitude by a Bessel function $J_2(2\pi B_M/PB^2)$, where P is the period of the oscillations. The consequence of the Bessel function modulation is that it reduces the signal amplitude at high fields and may introduce nodes at low fields depending upon the amplitude of B_M relative to P. As seen in Fig. 5, minima or nodal points in the observed oscillatory amplitude occur at ~ 11 and ~ 4.8 kG for $\mathbf{B}\|\langle 111 \rangle$, and at ~ 6.5 kG for $\mathbf{B}\|\langle 001 \rangle$; no minima could

TABLE I. Summary of samples investigated for beating effects. The period is expressed in units of 10^{-6} G^{-1} and N_0 is expressed in units of 10^{18} cm^{-3}.

Sample	$R_{4.2°K}$ (cm³/C)	Period	N_0	Current direction	Field orientation	Minima found B‖⟨111⟩ (kG)	B‖⟨001⟩ (kG)	$n = 1/PB$
24B	−3.2	2.48	1.46	⟨110⟩	Transverse	11	6.5	37.0
						4.8		84.7
58B-1	−3.2	2.48	1.46	⟨111⟩	Longitudinal	11	None seen at	37.0
						4.8	higher fields	84.7
							up to 150	
85C-2	−3.2	2.54	1.41	⟨100⟩	Transverse		6.4	
58B-2	−3.6	2.54	1.41	⟨110⟩	Transverse	None seen from 20 to 70		
80B-1	−3.9	2.58	1.37	⟨110⟩	Transverse	10		38.8
58B-3	−4.1	2.60	1.36	⟨110⟩	Transverse	10.1		38.1
58B-C	−4.6	2.70	1.28	⟨100⟩	Longitudinal	None seen from 20 to 190		
23B-3	−4.8	2.75	1.25	⟨110⟩	Transverse	9.5		38.3
80B-2	−5.0	2.82	1.20	⟨110⟩	Transverse	None seen down to ≈12		
23B-1K	−5.1	2.79	1.22	⟨111⟩	Longitudinal	8.8		40.4
23B-1N	−5.5	2.85	1.18	⟨111⟩	Longitudinal	8.6		40.8

be observed for $B‖⟨110⟩$. A detailed study indicates that the minima are not caused by the Bessel-function zeros.

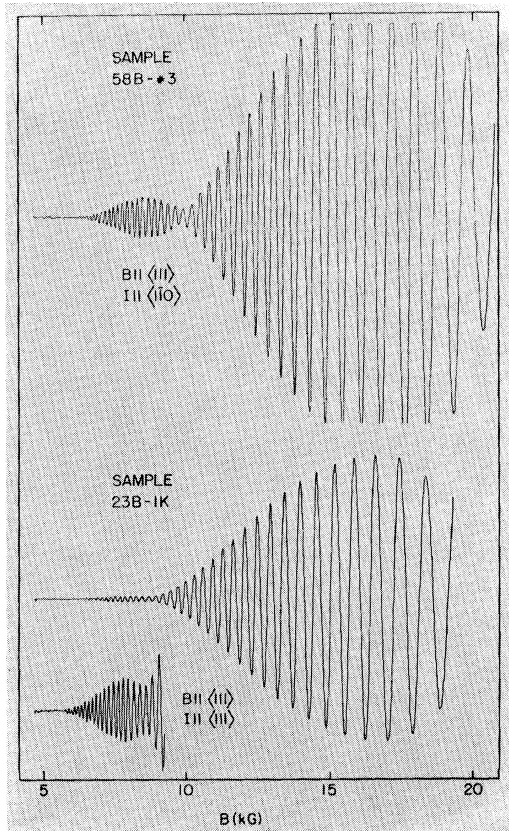It is not obvious that a phase shift in the sinusoidal oscillations occurs at the amplitude minima. However,

FIG. 6. Reproduction of x-y recorder traces of oscillatory magnetoresistance for samples 58B-3 and 23B-1K for $B‖⟨111⟩$. Large-amplitude recorder-pen excursions are clipped by the recorder for sample 58B-3.

a detailed investigation reveals that an approximately 180° phase shift in the oscillations take place both in the vicinity of the 11-kG minimum for $B‖⟨111⟩$ and in the vicinity of the 6.5-kG minimum for $B‖⟨001⟩$. This behavior was established by using two different methods. First, oscillatory data is taken for $B‖⟨111⟩$ or $B‖⟨001⟩$. Then, oscillatory data for a direction in which no minima are observed is also traced on the same x-y recorder sheet. For any field direction, it has been previously established that the period is independent of field strength at these low fields.[14] If the peaks of both tracings are approximately in phase at fields above the minima positions, they are then observed to be approximately 180° out of phase below the minima positions. Second, a careful frequency analysis of the raw data that was used in SB for measuring the frequency anisotropy shows that an approximately 180° phase shift occurs in the vicinity of the 11- and 6.5-kG minima.

Oscillatory data taken on two samples with slightly different carrier concentrations is shown in Fig. 6 for $B‖⟨111⟩$. As seen from this figure, the 11-kG node observed for sample 24B gradually shifts to lower fields as the concentration is lowered. A summary of samples investigated for beating effects is shown in Table I. In this table, N_0 is the concentration in the $k = 0$ conduction-band calculated from the SdH period under the assumption that the central band is spherical, and $n(= 1/PB)$ is the Landau-level number at which a node is seen in the oscillations for $B‖⟨111⟩$. Except for sample 24B, all the samples were cut from ingots whose growth axis was along a ⟨110⟩ direction. In the case of sample 24B, the ingot growth axis was along a ⟨111⟩ direction.

Beating patterns observed in n-HgTe[19] and gray-tin[18,20] which are not reproducible from sample to sam-

[19] S. H. Groves, R. N. Brown, and C. R. Pidgeon, Phys. Rev. 161, 779 (1967).
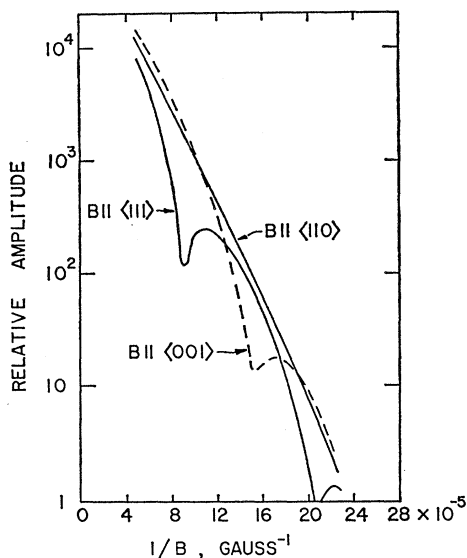[20] B. L. Booth and A. W. Ewald, Phys. Rev. 168, 805 (1968).

Fig. 7. Relative amplitude of SdH oscillations versus reciprocal magnetic field for sample 24B.

ple have been ascribed to inhomogeneities. The results given in Table I are reproducible from sample to sample. Booth[18] found that if his samples of gray-tin were re-etched, or if the samples were remounted, the beats would shift or be eliminated entirely. Reducing the dimensions of the sample, further etching, or remounting did not affect the positions of the minima or the oscillatory beat patterns in the samples of GaSb investigated. Inhomogeneity effects should not be important in GaSb for samples where the Fermi level is above the $\langle 111 \rangle$ valley band edge, since the Fermi-level position is stabilized by the large density of states in the $\langle 111 \rangle$ conduction band.[1] For samples where the Fermi level is below the $\langle 111 \rangle$ valley band edge, the decrease in lifetime of the $k=0$ electrons and the possible influence of inhomogeneities on the SdH amplitude prevent, to a large extent, observation of low-field minima in the oscillatory amplitude.

Figure 7 shows a plot of the relative amplitude of the SdH oscillations versus reciprocal magnetic field for
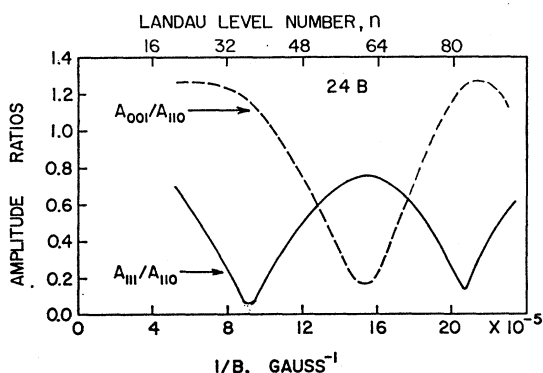

Fig. 8. Amplitude ratios versus $1/B$ or quantum number n for sample 24B.
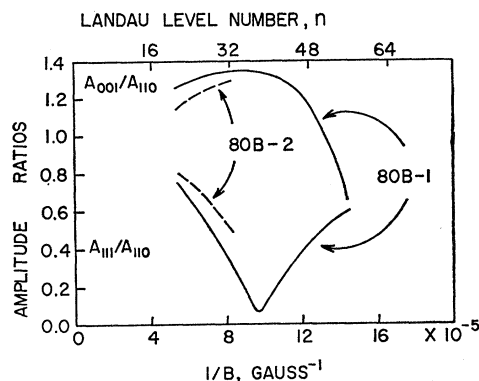

Fig. 9. Amplitude ratios versus $1/B$ for two lower-concentration samples 80B-1 and 80B-2. The quantum number n is shown for sample 80B-1.

sample 24B when the magnetic field is along the three principal crystallographic directions. The Bessel-function modulation of the amplitude may be calculated from a knowledge of the magnitude of the SdH period and the amplitude of the ac magnetic field. Dividing the observed SdH amplitude by this Bessel function yields the curves given in Fig. 7. As seen in the figure, the damping is approximately the same in each field direction, except for the effects of the beating. Figure 8 is then obtained by normalizing the amplitude behavior to the amplitude in the $\langle 110 \rangle$ field direction. This particular way of plotting the data separates the damping effects from the observed beating effects in a convenient manner. It can be seen from Fig. 8 that the ratio A_{001}/A_{110} is sometimes greater than 1.0, depending upon the magnetic field value; the ratio A_{111}/A_{110} is always less than 1.0 for fields in the range of this study. The amplitude at the nodal or minimum positions never goes completely to zero. This is probably partly due to the contribution of the second-harmonic SdH term to the oscillatory amplitude.

Amplitude-ratio plots are shown in Fig. 9 for two lower-concentration samples 80B-1 and 80B-2; the properties of these samples are listed in Table I. For $\mathbf{B}\|\langle 111\rangle$, a minimum is seen at about 10 kG in sample 80B-1. In sample 80B-2, the damping of the oscillations at low fields prevents the observation of a minimum, but the
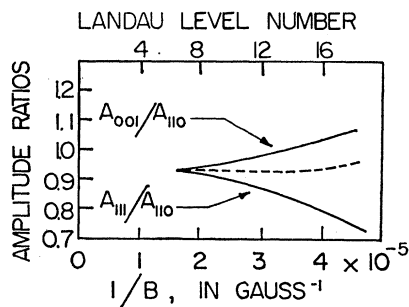

Fig. 10. Amplitude ratios versus $1/B$ for sample 58B-2 for fields up to about 70 kG.

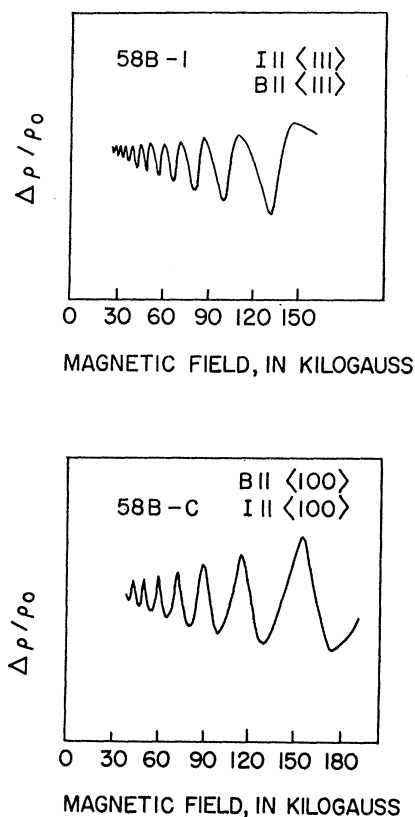MAGNETIC FIELD, IN KILOGAUSS

MAGNETIC FIELD, IN KILOGAUSS

FIG. 11. Longitudinal oscillatory magnetoresistance on samples 58B-C and 58B-1 using pulsed magnetic fields up to 190 kG (see Ref. 21).

decrease in the amplitude ratio indicates that a minimum is present at lower fields. When the magnetic field is parallel to an $\langle 001 \rangle$ direction, the amplitude ratio for both samples reaches a maximum (greater than 1.0) and then decreases slightly at the higher fields. The Landau-level numbers n shown in Fig. 9 are calculated for sample 80B-1.

Figure 10 shows amplitude ratio results on sample 58B-2 for fields up to approximately 70 kG at 4.2°K. The amplitude ratios appear to approach the same limiting value, ~ 0.93, at high fields. The dashed line in Fig. 10 represents the amplitude ratio $A_{25°}/A_{110}$, where $A_{25°}$ is the oscillatory amplitude when the magnetic field is along a direction 25° away from the $\langle 001 \rangle$ axis in the (110) plane.

The longitudinal oscillatory magnetoresistance has been investigated[21] using pulsed fields up to about 190 kG on sample 58B-C and up to 150 kG on sample 58B-1. As seen in Fig. 11, no deviations from the usual approximately exponential behavior of the amplitude of the oscillations can be seen for either of these two different field directions.

Figure 12 shows the variation of the Landau-level number at which a nodal point or minimum occurs

versus the magnetic field direction for samples 24B and 80B-1. As seen in Fig. 12, the high-field nodal point is approximately symmetric around the $\langle 111 \rangle$ direction, whereas the low-field nodal point is asymmetric around the $\langle 111 \rangle$ direction. An alternate presentation of the data for sample 24B, as seen in Fig. 13, shows the relative amplitude and nodal positions as a function of field direction for various values of magnetic field. The relative amplitudes are normalized to the amplitude at 6 kG by multiplying the observed amplitude at a particular field value B_p by the Bessel-function ratio

$$\frac{J_2(2\pi B_M / P(6 \text{ kG})^2)}{J_2(2\pi B_M / P B_p^2)} .$$

Also given is the approximate value of the magnetic quantum number n, or the Landau-level number.

A plot of B_0 (the value of the field at which the higher field minimum is seen for $\mathbf{B}\|\langle 111 \rangle$) versus electron concentration in the $\mathbf{k}=0$ conduction band is shown in Fig. 14 for a number of samples listed in Table I. The nodal point position is seen to be linear in the concentration in the range investigated. Additional data have been obtained using hydrostatic stress[22] and uniaxial compressional stress.[23] Again, B_0 is seen to decrease with concentration. In the case of uniaxial stress, the decrease in B_0 is more rapid than at zero stress. For the case of hydrostatic stress, the concentration variation was not established because only the end points could be measured. After application of hydrostatic stress to sample 24B, beating could only be seen for $\mathbf{B}\|\langle 111 \rangle$. From the uniaxial stress results, we assume that the hydrostatic
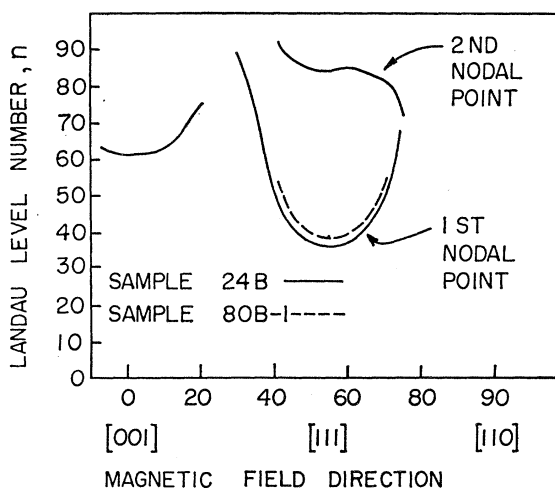

MAGNETIC   FIELD   DIRECTION

FIG. 12. Variation of Landau-level number n at which a nodal point occurs versus the magnetic field direction for samples 24B and 80B-1.

[21] N. T. Sherwood (private communication).

[22] The "ice-bomb" technique was used to generate hydrostatic pressures at low temperatures. For a description of the apparatus, see D. G. Seiler and W. M. Becker, Phys. Rev. 186, 784 (1969).
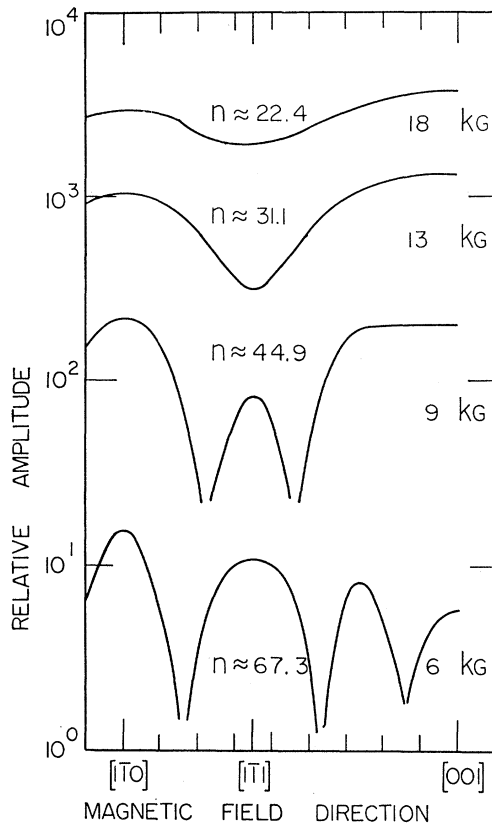
[23] D. G. Seiler and N. T. Sherwood (unpublished).

FIG. 13. Relative amplitude as a function of magnetic field direction for sample 24B.

pressure result represents motion of the ~ 11 kG minimum to lower fields.

V. DISCUSSION

A. Inadequacy of Classical Theory

The classical theory predicts a beating effect to occur if the two extremal cross-section areas are unequal in certain directions. The analysis of the beating patterns would then be expected to yield the magnitude of the area differences between the two electron orbits. The following series of experiments indicate that the two low-field nodes observed with $\mathbf{B}\|\langle 111\rangle$ for high-concentration material are not related to a simple beating behavior between two nearly equal frequencies:

(1) For sample 24B (the highest-concentration sample investigated) two minima, with a node spacing of about 48 oscillations, are observed for $\mathbf{B}\|\langle 111\rangle$ (see Fig. 5). On the basis of a classical model, the two Fermi-surface cross sections would be expected to differ by about 2%. In 58B-1, a sample with about the same carrier concentration as 24B, the oscillatory behavior in the longitudinal orientation ($\mathbf{I}\|\langle 111\rangle$, $\mathbf{B}\|\langle 111\rangle$) has been measured at low fields (electromagnet; 4–20 kG), intermediate fields (super-conducting solenoid; 15–70 kG),

and finally at high fields (pulse field system; 30–190 kG). The two nodes seen in 24B were also detected in sample 58B-1. On the basis of a classical model, an antinode would have been expected to occur at about 31 kG in these samples. No amplitude variation identifiable as an antinode is observed around this field position in 58B-1 or 24B. In fact, no evidence of a significant deviation of the amplitude from exponential dependence on field is seen for fields above ≈ 20 kG.

(2) In Fig. 12, it is seen that as the magnetic field is rotated away from the $\langle 111\rangle$ direction toward the $\langle 110\rangle$ direction the two low-field nodes approach each other. In sample 24B, at $\theta = 74°$, the observed nodal positions are very close together (~ 12 oscillations apart). One would then expect to see several more nodal points in the field range of measurement if the nodes observed for $\mathbf{B}\|\langle 111\rangle$ are connected by simple beating. No such additional nodes are seen.

A study of the de Haas–van Alphen and Shubnikov–de Haas effects in n-HgSe in pulsed fields up to 210 kG was recently made by Bliek and Landwehr.[24] Their study was confined to a magnetic field orientation along a $\langle 100\rangle$ direction and to samples with electron concentrations between 1.96 and 3.26×10^{18} cm^{-3}. Their results showed that no beating effects could be observed (except for the previously mentioned nodes first seen by Whitsett[7]) at these high magnetic fields. They concluded from this that the observed beating effects are not caused by simple beating from two nearly equal frequencies.

The two nodes for $\mathbf{B}\|\langle 111\rangle$ in GaSb may reflect the presence of different groups of carriers in different regions of the Brillouin zone. If the 11-kG node is due to beating between carriers in the central minimum and the low-mass component of the carriers in the $\langle 111\rangle$ valleys, a small decrease in concentration when the
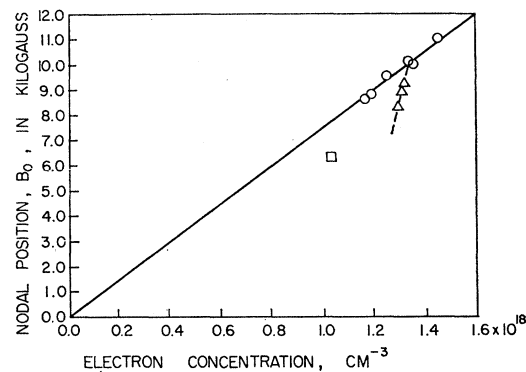

FIG. 14. Plot of B_0 versus carrier concentration in the $\mathbf{k}=0$ minimum. The circles represent data taken at atmospheric pressure. The square represents the ice-bomb result on sample 24B. The triangles are points taken on sample 58B-3 using uniaxial compressional stress along the $\langle 110\rangle$ direction. (In all cases, the concentration is calculated directly from the SdH period.)

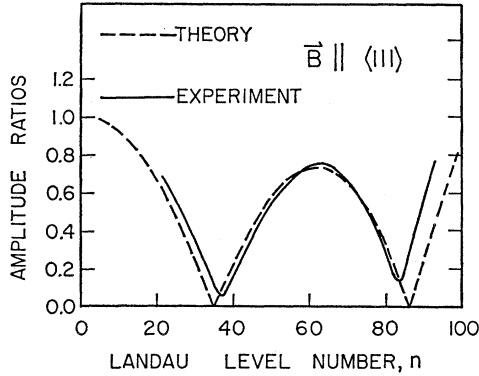[24] L. M. Bliek and G. Landwehr, Phys. Status Solidi **31**, 115 (1969).

FIG. 15. Plot of theoretical and experimental
amplitude ratios for $\mathbf{B}\|\langle 111\rangle$.

Fermi level is in the vicinity of the $\langle 111\rangle$ valley band
edge should produce rapid motion of the 11-kG mini-
mum. Instead, the 11-kG minimum appears to shift
only slowly with change in concentration. The shift of
the 4.8-kG minimum with concentration could not be
investigated by the present techniques. Recent measure-
ments by Mashovets, Parfen'ev, and Vekshina[5] indicate
that SdH contributions from the $\langle 111\rangle$ valleys are ob-
servable at extremely high fields. At low fields, however,
oscillatory contributions from the $\langle 111\rangle$ valley carriers
should be highly damped since the transverse mass in
this band is still very large compared to the mass of
the $\mathbf{k}=0$ carriers.

Zhang and Callaway[25] have made an energy-band
calculation for GaSb using an empirical pseudopoten-
tial which was nonlocal and included spin-orbit coupling.
More recently, Zhang[26] analyzed the shape of the $k=0$
conduction band based on this calculation. In this work,
the inversion asymmetry term is written as $E_3 T_3 k^3$,
where T_3 is the same as $f_2(\mathbf{k})/k^3$ in our notation. Zhang
found a value of $E_3 = 0.0503364$ in units employed in his
paper, which corresponds to -4.56×10^{-23} eV cm³. E_3
is equivalent to our $w\hbar^2/2m_0 k$ so that Zhang predicts
$w=0.42$ and $C_2 = 0.05$ $w=0.021$, using an effective mass
of 0.05 m_0. The classical beat period from $C_2 = 0.021$ is
14.6×10^{-5} G^{-1}, which compares favorably with the
observed $\langle 111\rangle$ node separation of 11.7×10^{-5} G^{-1} as it
should on a classical model. (Zhang actually calculates
16.5×10^{-5} G^{-1}; the difference between the two results
is not clear.) However, in Sec. V B, we shall see that
quantum effects worsen the agreement with Zhang's
theory.

B. Fit to Quantum-Mechanical Theory

The two low-field nodal points seen in sample 24B do
not appear to be related by simple beating. The analysis
given in R in explaining the beating effects in HgSe
indicates that magnetic interaction between Landau

levels should be taken into account in predicting and
analyzing the beating effects observed in GaSb.

Figure 4 shows the results of a computer calculation
giving the function $A_s(n)$ which includes this magnetic
interaction. The g value was taken to be -6,[4,27] and so
$\mu = 0.575$. Then the value of $C_2 = 0.05$ was chosen to give
the best fit to the experimental nodes. In order to com-
pare this theoretical calculation with the experimental
results, it is necessary to plot amplitude ratios. For the
field along a $\langle 110\rangle$ direction, $m^*=0.05m_0$, $g=-6$, the
function $A_s(n)$ is given by

$$A_s(n) = \cos(\pi g m^*/2m_0) \approx 0.89,$$

independent of n. Theoretical amplitude ratios can then
be formed by dividing 0.89 into the $A_s(n)$ values for the
two cases $\mathbf{B}\|\langle 111\rangle$ and $\mathbf{B}\|\langle 100\rangle$. These theoretical ratios
can then be compared with the experimental amplitude
ratios shown previously in Fig. 8. Figures 15 and 16
show the comparison of the theoretical and experimental
amplitude ratios for $\mathbf{B}\|\langle 111\rangle$ and $\mathbf{B}\|\langle 100\rangle$, respectively.
These figures show that the theory given in R quite
strikingly is able to reproduce the main features of the
experimental data. The theory predicts that A_{001}/A_{110}
$=A_{111}/A_{110}$ at high fields, which is verified for the data
taken on sample 58B-2 shown in Fig. 10. However, the
theory predicts that these ratios should equal a value of
1.0 at high fields and not a value of ~0.93 as seen in
Fig. 10. Since high-field data was taken on only one
sample in the superconducting magnet, this unexplained
result warrants a further more careful investigation of
the amplitude ratios at high fields. From this data, one
could, in principle, extract the size of the anisotropy of
the electron g factor.

From the value of C_2 of 0.05, we can calculate several
quantities for sample 24B. According to Eq. (27), the
maximum energy splitting at the Fermi level is $C_2 E_F$
or 0.005 eV (from $E_F \cong 0.096$ eV), and the maximum
radial splitting of the two energy surfaces is $2\frac{1}{2}\%$. An
estimate of the higher-band parameter B' can be made
from the magnitude of C_2 for sample 24B by using Eqs.
(6) and (12). The coefficients a_4 and b_4 can be evaluated
by the techniques outlined in Appendix B in SB. For
sample 24B, $a_4 = 0.953$ and $b_4 = 0.076$; thus, $B' = 9.6$ in
units of $\hbar^2/2m_0$. This value is of the same order of mag-
nitude as the estimate of $B' = 12$ made in RGW for
HgSe, assuming that the HgSe conduction band has Γ_6
symmetry.

We can compare the separation between nodes in the
$\langle 111\rangle$ case to the classical beat period. Classically, the
beat period relative to the SdH period is $(C_2 g_2(\theta)/\pi)^{-1}$,
or 24.8 oscillations for the 24B sample, using the C_2
value derived from the quantum-mechanical fit. This
is to be compared with 47.7 oscillations from Table I.

[25] H. I. Zhang and J. Callaway, Phys. Rev. **181**, 1163 (1969).
[26] H. I. Zhang (unpublished).

[27] E. J. Johnson, I. Filinski, and H. Y. Fan, in *Proceedings of
the International Conference on the Physics of Semiconductors,
Exeter* (The Institute of Physics and the Physical Society, London,
1962), p. 375; E. J. Johnson and H. Y. Fan, Phys. Rev. **139**,
A1991 (1965).

Thus the quantum effects increase the separation of these two nodes by a factor of 2. In terms of G^{-1}, the quantum effect predicts a classical beat period of 5.85×10^{-5} G^{-1}, as compared with the observed node separation of 11.7×10^{-5} G^{-1}. Zhang's energy-band calculation yields a value of 16.5×10^{-5} G^{-1} for the classical beat period. The present considerations show that this should be compared with 5.85×10^{-5} rather than 11.7×10^{-5}, so that the results differ by almost a factor of 3. Thus, Zhang's value for C_2 or B' would be a factor of 3 too small.

C. Other Features of Results

In Fig. 12 is shown the angular variation of the nodal point position versus the magnetic field direction for sample 24B. The calculations in R were made only for $\mathbf{B} \| \langle 100 \rangle$, $\langle 110 \rangle$, and $\langle 111 \rangle$. For other field directions, the Hamiltonian is complicated and has not been solved as yet. However, it is interesting to notice that the position of the $\langle 111 \rangle$ nodal point with the smallest n value almost follows the classical result of Fig. 2, at least in the regions around the $\langle 111 \rangle$ and $\langle 100 \rangle$ directions. The position of the second node shows, as we have noted previously, distinctly nonclassical behavior.

Turning now to Fig. 14, the plot of B_0 and the first $\langle 111 \rangle$ node versus concentration, we first note that classically B_0 should be proportional to $C_2 F_0$, i.e., the classical beat frequency. The same proportionality holds approximately in the quantum-mechanical picture, as was found in R. Now for spherical bands, F_0 should go as k^2, and since for small enough k the inversion asymmetry term goes as k^3, C_2 must go as k. Therefore, B_0 should be proportional to k^3, and the plot against the concentration, which also goes as k^3, should give a straight line through the origin. The agreement is actually quite good.

Hydrostatic and uniaxial compressional stress studies on several samples of high-concentration n-GaSb show that the beating patterns change with applied stress. The nodal points seen along the $\langle 111 \rangle$ and $\langle 100 \rangle$ field
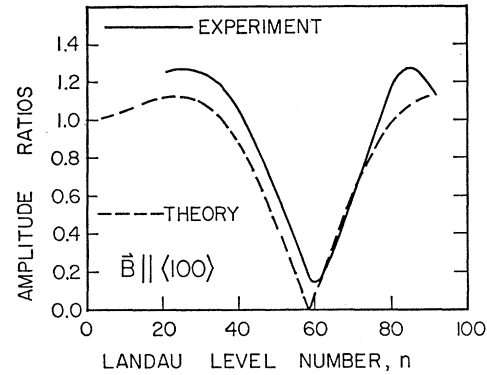

FIG. 16. Plot of theoretical and experimental amplitude ratios for $\mathbf{B} \| \langle 100 \rangle$.

directions are observed to move to lower fields as a function of increasing stress. Since the stress moves the Γ_1 band edge closer to the L_1 valley band edges, carriers are transferred from the Γ_1 band to the L_1 valleys, which decreases the concentration in the $\mathbf{k} = 0$ minimum. However, as can be seen in Fig. 14, the motion of the nodal point with stress is inconsistent with the data on the concentration dependence of the nodal points at atmospheric pressure. These deviations are not understood at present.

It may be concluded that the beating effects observed in n-GaSb are due to the inversion-asymmetry splitting of the conduction band. The experimental evidence indicates that the beating is not simple, and, thus, cannot be explained on the basis of classical arguments alone. The quantum-mechanical theory, which includes the interaction between the electron spin and external magnetic fields, accounts for many of the major features of the data.
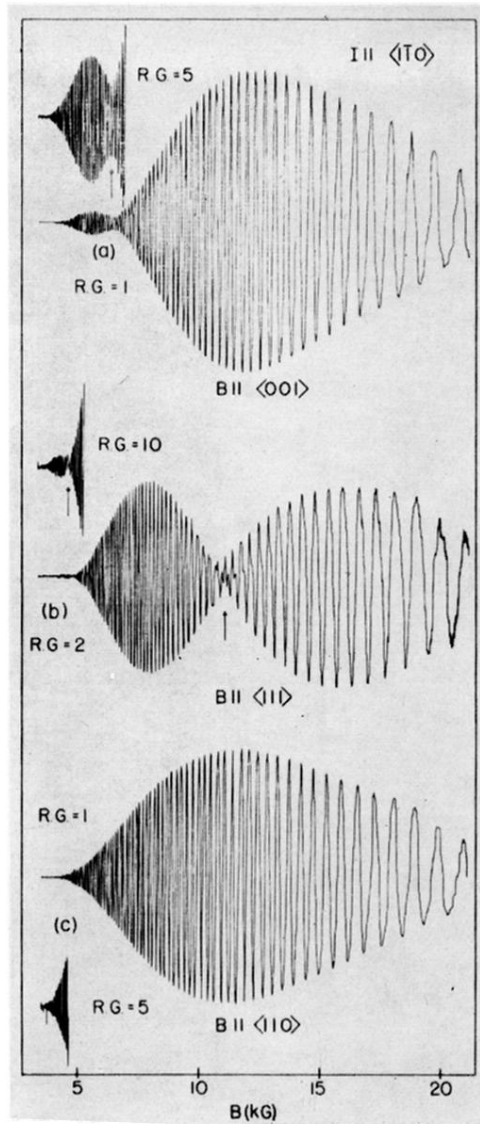
ACKNOWLEDGMENTS

FIG. 5. Reproduction of *x-y* recorder traces of oscillatory magnetoresistance data taken on sample 24B while detecting at the second harmonic of the modulation frequency. The RG of each trace is indicated. This figure is taken from Ref. 6, Fig. 1.
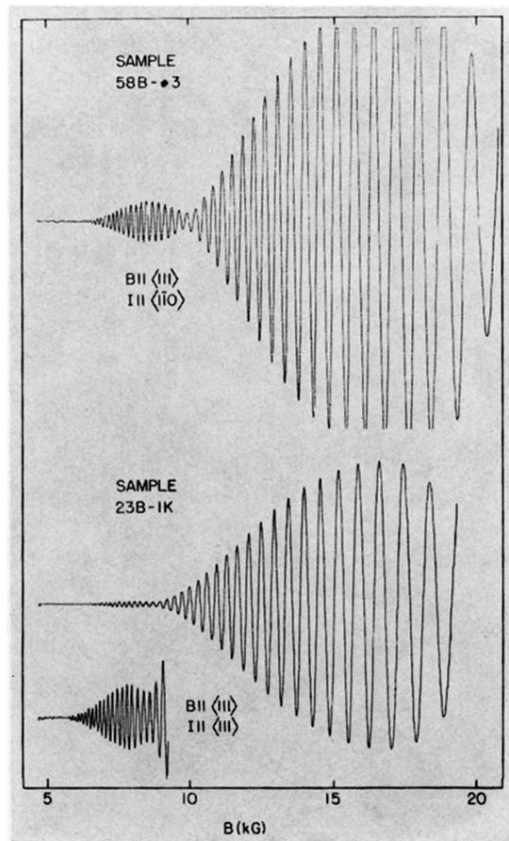
FIG. 6. Reproduction of *x-y* recorder traces of oscillatory magnetoresistance for samples 58B-3 and 23B-1K for $\mathbf{B}\|\langle 111\rangle$. Large-amplitude recorder-pen excursions are clipped by the recorder for sample 58B-3.